International Journal of
Molecular Sciences

MDPI

Article

Novel Spinel Li–Cr Nano-Ferrites: Structure, Morphology, and Electrical/Dielectric Properties

Mukhametkali Mataev [1], Altynai Madiyarova [1,*], Moldir Abdraimova [1,*], Marzhan Nurbekova [1], Karima Seibekova [1], Zhanar Tursyn [1], Assel Kezdykbayeva [2], Krishnamoorthy Ramachandran [3] and Bahadir Keskin [4]

[1] Department of Chemistry, Faculty of Natural Sciences, Kazakh State Women's Teacher Training University, Almaty 050000, Kazakhstan; mataev.m@qyzpu.edu.kz (M.M.); nurbekova.m@qyzpu.edu.kz (M.N.); seitbekova.k@qyzpu.edu.kz (K.S.); tursyn.zh@qyzpu.edu.kz (Z.T.)
[2] Departments of Inorganic and Technical Chemistry, Faculty of Chemistry, E.A. Buketov Karaganda State University, Karagandy 100024, Kazakhstan; kezdikbayeva_assel@buketov.edu.kz
[3] Department of Physics, SRM Institute of Science and Technology, Vadapalani Campus, Chennai 600026, India; ramachak1@srmist.edu.in
[4] Department of Chemistry, Faculty of Arts & Science, Yildiz Technical University, TR34220 Istanbul, Turkey; bahadirkeskin@gmail.com
* Correspondence: madiyarova.a@qyzpu.edu.kz (A.M.); abdyraimova.m@qyzpu.edu.kz (M.A.); Tel.: +7-702-660-29-92 (A.M.)

Abstract

This article reports on the synthesis and physicochemical characterization of a novel complex ferrite material, $LiCr_{3.4}Fe_{1.6}O_8$, prepared via the sol-gel method. X-ray diffraction (XRD) analysis confirmed that the synthesized compound is a single-phase material with a spinel-type structure and cubic symmetry. Raman spectroscopy was employed to investigate the vibrational modes, and the observed peaks corresponding to Fe–O and Cr–O bonds further validated the spinel-like structure of the compound. The microstructure and elemental composition were examined using scanning electron microscopy (SEM). Multiple regions of the $LiCr_{3.4}Fe_{1.6}O_8$ crystals were analyzed, revealing a homogeneous phase and providing detailed insight into the morphology and chemical composition of the surface. The synthesized ferrite particles exhibited relatively large dimensions, with sizes measured at approximately 5, 30, 100, and 200 μm. The dielectric behavior was studied to assess the material's response to an external electric field, demonstrating its capacity for electric charge polarization. Both capacitance and electrical conductivity were found to increase with rising temperature. Electrophysical measurements were conducted using the LCR-800 system over a temperature range of 293–483 K and at frequencies of 1.5 kHz and 10 kHz. An increase in frequency to 10 kHz resulted in a decrease in the dielectric constant (ε) across the entire temperature range.

Keywords: sol-gel method; ferrites; symmetry; X-ray diffraction; pycnometric density; unit cell parameters; scanning electron microscope

check for updates

Academic Editor: José Luis Toca-Herrera

Received: 24 September 2025
Revised: 19 October 2025
Accepted: 24 October 2025
Published: 26 October 2025

Citation: Mataev, M.; Madiyarova, A.; Abdraimova, M.; Nurbekova, M.; Seibekova, K.; Tursyn, Z.; Kezdykbayeva, A.; Ramachandran, K.; Keskin, B. Novel Spinel Li–Cr Nano-Ferrites: Structure, Morphology, and Electrical/Dielectric Properties. *Int. J. Mol. Sci.* **2025**, *26*, 10409. https://doi.org/10.3390/ijms262110409

Copyright: © 2025 by the authors. Licensee MDPI, Basel, Switzerland. This article is an open access article distributed under the terms and conditions of the Creative Commons Attribution (CC BY) license (https://creativecommons.org/licenses/by/4.0/).

1. Introduction

Despite the rapid advancement in the field of materials science in recent years, there are still many unresolved issues. These include materials with perovskite, spinel, ferrite-garnet, and garnet-type structures [1]. Various methods are employed for obtaining multiferroic materials, including sol–gel, high-temperature solid-state synthesis, hot soap, spray pyrolysis, co-precipitation, and combustion techniques [2–12]. Among them, nano-sized ferrite

particles are of particular interest due to their unique properties and wide range of applications. Ferrite materials have been widely used in numerous technological applications, including magnetically controlled drug delivery for cancer therapy, color imaging, gas sensing materials, and catalytic materials [13–20].

Spinel ferrite magnetic ceramics are gaining increasing attention in the electronics industry due to their exceptional properties, including high magnetic permeability, low dielectric losses, moderate saturation magnetization, strong magnetic induction, mechanical hardness, low eddy current losses, and ease of processing [21–26]. The demand for ferrites continues to grow rapidly, driven by their wide range of applications in fields such as biomedicine, targeted drug delivery, electromagnetic wave absorption, catalysis, computer memory systems, magnetic recording, and switching devices [27,28].

Among these, lithium (Li) ferrite stands out as a highly promising material for microwave technologies and is extensively used in electronic and communication systems [29]. Lithium ferrites are regarded as some of the most versatile ferrite materials due to their wide application spectrum. Owing to their excellent rectangular hysteresis loops, they are commonly utilized in data storage systems, switching components, and phase shifters [30–32]. With a relatively high Curie temperature of around 640 °C, lithium ferrites can operate effectively across a broad range of technically important temperatures. At room temperature, lithium ferrites offer better conductivity and higher saturation magnetization than yttrium iron garnet, while also being more cost-efficient. Moreover, they are widely used in lithium-ion batteries [33,34]. Lithium ferrite ($Li_{0.5}Fe_{2.5}O_4$) is also recognized as a valuable material for use in construction and engineering sectors [35].

Among the various synthesis methods, the sol–gel technique is considered particularly effective and straightforward, as it allows for material formation at relatively low agglomeration temperatures. This method offers several benefits, including the use of low-cost precursors, operational simplicity, energy efficiency, and the ability to produce nanoparticles with fine, controlled structures.

The primary aim of this study is to explore the potential of lithium ferrites ($Li_{0.5}Fe_{2.5}O_4$) in a variety of applications, including energy storage electrodes (such as those used in lithium-ion batteries), magnetic core inductors, military stealth technologies, and multilayer components in electronic devices. Accordingly, the investigation of synthesis parameters, X-ray structural analysis, and studies of the thermodynamic, physicochemical, and magnetic properties of these materials remain areas of significant scientific interest. This work presents a comprehensive investigation into the synthesis and characterization of ferrite nanoparticles using various preparation techniques.

2. Results

2.1. X-Ray Diffraction (XRD) Analysis

The XRD pattern of the synthesized $LiCr_{3.4}Fe_{1.6}O_8$ complex ferrite was recorded at room temperature. As illustrated in Figure 1, the diffraction results confirm the complete transformation of the sample from an amorphous to a fully polycrystalline state, with the formation of a well-defined single phase. All observed peaks correspond to specific crystallographic planes, indicating the presence of a spinel-type cubic structure with space group $Fd\bar{3}m$.

The X-ray analysis also showed that the lattice parameter of the $LiCr_{3.4}Fe_{1.6}O_8$ ferrite is influenced by the calcination conditions. The absence of secondary or impurity phases in the diffraction pattern attests to the high purity and structural quality of the synthesized material. The X-ray pattern card number is No. 04-010-5163.

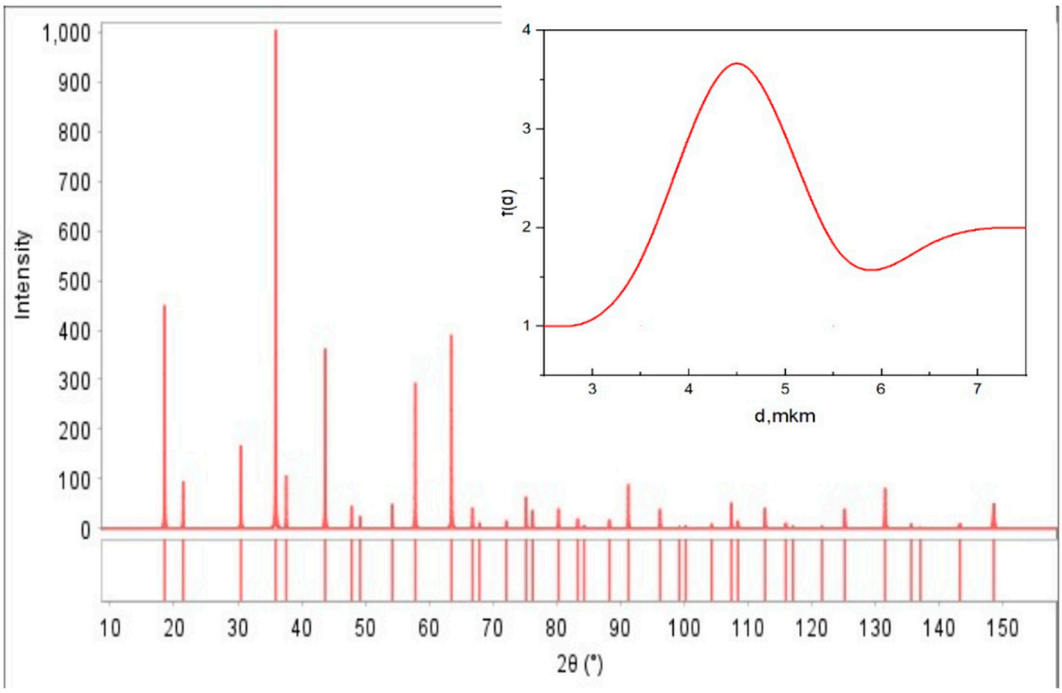


Figure 1. X-ray diffraction pattern of the complex ferrite $LiCr_{3.4}Fe_{1.6}O_8$.

The figure above depicts the unit cell of the crystal structure. A unit cell represents the smallest repeating structural element in a crystalline material. In this case, the cell exhibits a cubic geometry, reflecting the material's high degree of symmetry. Lithium (Li) and Chromium (Cr) atoms are shown in the same color, indicating that they are statistically distributed over identical crystallographic sites.

Lithium atoms are positioned at the tetrahedral sites, each surrounded by four oxygen atoms, while Chromium and Iron (Fe) atoms occupy octahedral sites, where they are coordinated by six oxygen atoms. The lines connecting the atoms represent the chemical bonds that maintain the integrity of the structure, which are predominantly ionic in nature.

The $Fd\bar{3}m$ space group is a defining feature of spinel structures. Figure 2 shows the crystal structure of the complex ferrite $LiCr_{3.4}Fe_{1.6}O_8$, which belongs to the $Fd\bar{3}m$ space group. In the case of the $LiCr_{3.4}Fe_{1.6}O_8$ compound, this crystallographic symmetry significantly influences its physical and chemical properties by determining the precise atomic arrangement and electronic structure. Such a configuration also has a pronounced effect on the magnetic properties of the material.

Below, the results of the Rietveld refinement based on the X-ray diffraction data for the synthesized complex ferrite are presented.

The reliability of the structural analysis is supported by the close agreement between the X-ray density and the values obtained from pycnometric measurements.

Elevated temperatures can contribute to the removal of structural defects or residual impurities, thereby enhancing crystal quality and promoting the growth of larger crystallites. The average crystallite size was estimated using the Debye–Scherrer equation, which is commonly used to determine crystallite dimensions from X-ray diffraction peak broadening. The Scherrer formula used for this calculation is as follows:

$$d = \frac{K\lambda}{\beta \cos\theta} \quad (1)$$

where

d—average size of crystals;

K—dimensionless particle shape coefficient (Scherrer constant);
λ—wavelength of X-ray radiation;
β—half-height reflex width (2θ in radians and units);
θ—diffraction angle (Bragg angle).

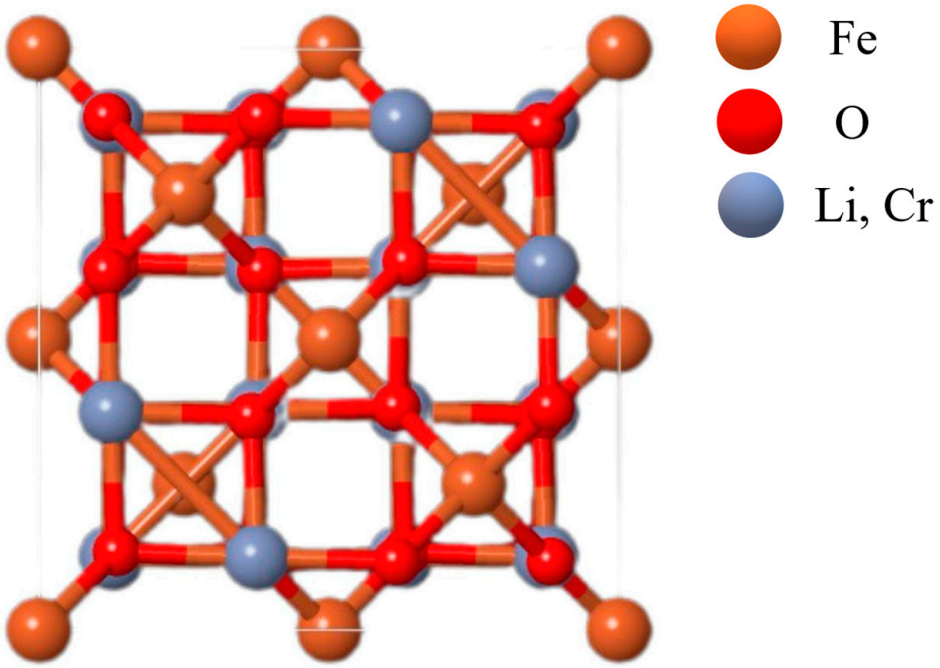


Figure 2. Crystal structure of the complex ferrite $LiCr_{3.4}Fe_{1.6}O_8$ with space group $F\bar{d}3m$.

The microstructural characteristics, including crystallite size and microstrain, of the synthesized complex ferrite were determined using the Williamson–Hall (W–H) method. The Williamson–Hall equation is a widely used analytical approach for examining crystal structures and their mechanical properties. It enables the evaluation of microstructural features—specifically, the average crystallite size and lattice strain—based on data derived from X-ray diffraction analysis. The W–H equation is expressed as follows:

$$\beta cos\ \theta = \frac{\kappa\lambda}{D} + 4\varepsilon sin\ \theta \quad (2)$$

where:

β—Full width of the diffraction peak (also called "width") in radians,
θ—Diffraction angle,
k—A system factor required for the calculation (usually taken as 0.9),
λ—Wavelength of the X-ray radiation,
D—Average crystallite size (sometimes referred to as "crystal size"),
ϵ—Effect of internal strain, i.e., the expansion and compression due to stresses within the crystal.

To determine these parameters, a plot was constructed based on the relationship between βcos θ and 4sin θ, as illustrated in Figure 3. By applying linear regression to this plot, the slope of the line provides the microstrain, while the y-intercept corresponds to the crystallite size, as summarized in Table 1. The analysis was conducted using the Uniform Deformation Model (UDM), which assumes uniform strain in all crystallographic directions, indicating that the material exhibits isotropic behavior.

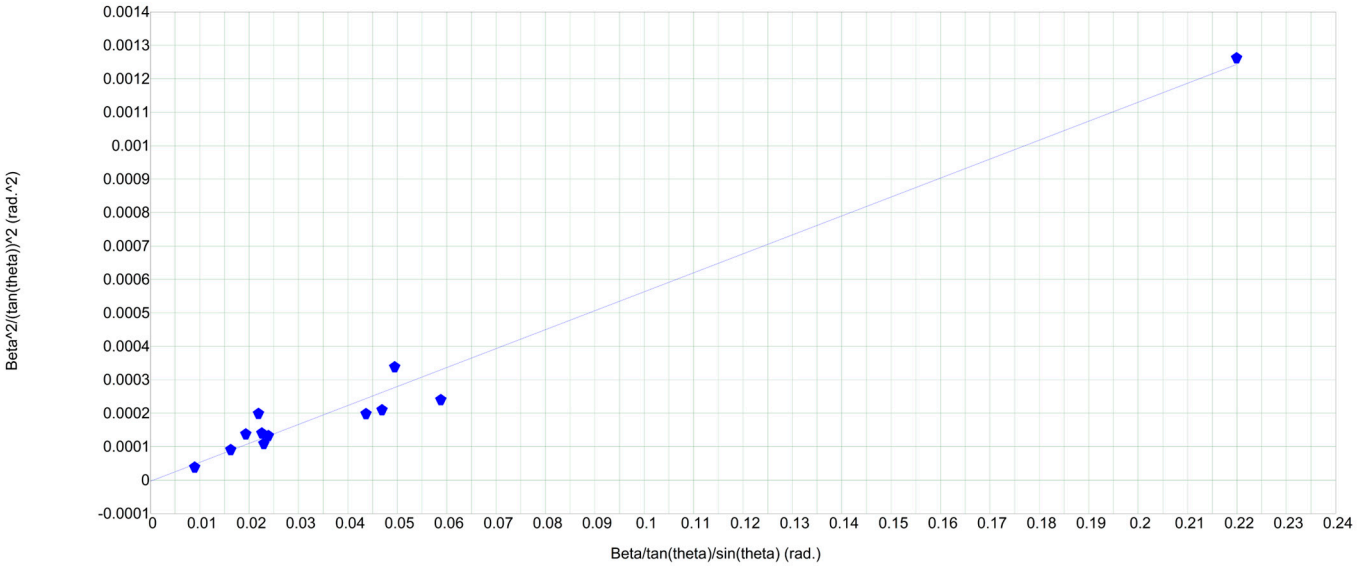


Figure 3. Williamson-Hall (W-H) plot of the $LiCr_{3.4}Fe_{1.6}O_8$ complex ferrite.

Table 1. This is a table. Structural parameters of $LiCr_{3.4}Fe_{1.6}O_8$ obtained by Rietveld refinement of X-ray diffraction data.

Sample	$LiCr_{3.4}Fe_{1.6}O_8$
Space Group	$Fd\bar{3}m$, the cubic side is centered
Z	4
Cell Parameter (Å)	
a =	8279 Å
b =	8279 Å
c =	8279 Å
V(Å^3)	57.646 Å^3
Agreement factors	
R-factor	0.036
I/Ic	3.67
I/Ic- CW ND	0.76
α	90
β	90
γ	90
X-ray density (g/cm^3)	4.694 g/cm^3
Pycn.density (g/cm^3)	4.695 g/cm^3

The crystallite sizes calculated using the Williamson–Hall method were slightly larger than those obtained from the Scherrer equation. This difference is primarily attributed to lattice strain induced by varying heat treatment temperatures [36–40]. As shown in Table 2, increasing the calcination temperature results in a decrease in lattice strain, which facilitates recrystallization and grain growth, thereby reducing structural defects and internal stresses.

Table 2. Average crystallite size and average strain for all ferrite samples fired at different temperatures, according to the Scherrer and W-H methods.

Sample	Scherrer Method	Williamson-Hall Method	
	D (nm)	D (nm)	$\varepsilon \times 10^{-3}$
$LiCr_{3.4}Fe_{1.6}O_8$	5.2	9.12	1.71

2.2. Raman Spectroscopy

Raman spectroscopy was employed to analyze the phase structure and composition of the modified samples. This technique identifies the vibrational modes of molecules through molecular spectroscopy.

The measurements were performed using a SPECTRUM TERS system. A solid-state laser with a wavelength of 473 nm and a maximum power output of 35 kW was used for excitation, focusing on a laser spot of approximately 2 μm in diameter on the sample surface. The Raman signal was collected in backscattering geometry using an SSD detector, while the sample was cooled to −65 °C. The spectral resolution of the 600/600 grating was 4 cm^{-1}, with a signal accumulation time of 30 s.

The *Y*-axis represents normalized intensity, enabling the comparison of relative Raman signal strengths across different spectra. The *X*-axis indicates the Raman shift in cm^{-1}, which corresponds to the vibrational energy levels of the molecules within the sample.

Figure 4 shows three Raman spectra. Peaks near the 200 cm^{-1} region (at 195, 200, and 206 cm^{-1}) are attributed to lattice vibrations involving Li^{+}, Cr^{3+}, or Fe^{3+} cations. In the 500–600 cm^{-1} range (509, 511, 516, 597 cm^{-1}), the peaks correspond to Fe–O bond vibrations within the spinel lattice. Peaks observed between 600 and 700 cm^{-1} (at 608, 618, 650, 690, and 705 cm^{-1}) relate to Fe–O vibrational modes in ferrite groups, especially those involving CrO_4^{2-} units. A prominent peak around 720 cm^{-1} signals a high concentration of ferrite groups.

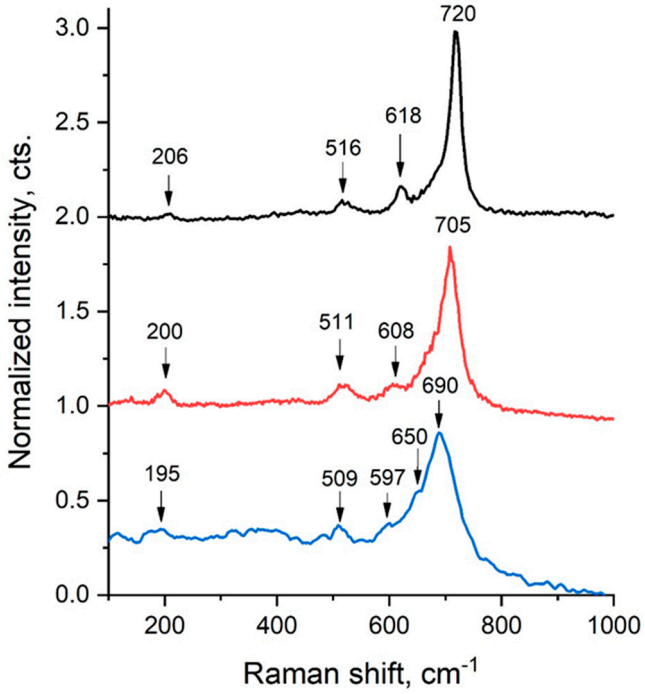


Figure 4. Raman Spectrum of the $LiCr_{3.4}Fe_{1.6}O_8$ Sample.

The detection of characteristic Fe–O and Cr–O vibrational peaks confirms that the $LiCr_{3.4}Fe_{1.6}O_8$ sample has a spinel-type crystal structure. Variations in peak intensity and position among the three spectra suggest sample heterogeneity or differences in crystallite orientation in different regions. In addition, the colors (black, red, and blue lines) generally represent $LiCr_{3.4}Fe_{1.6}O_8$ ferrite samples obtained at different calcination temperatures. The blue line corresponds to the sample synthesized at a lower temperature, the red line represents the sample prepared at a medium temperature, and the black line indicates the sample obtained at a higher temperature.

As the temperature increases, the shift and intensity of the peaks change—this indicates the improvement of the crystalline structure, the strengthening of ionic bonds, or possible phase transitions.

Overall, the Raman spectrum of the $LiCr_{3.4}Fe_{1.6}O_8$ sample indicates a complex phase composition, consisting of both spinel structures and ferrite groups.

Raman (or combination scattering) spectroscopy provides a graphical representation of light scattering resulting from its interaction with molecules in a material. While Rayleigh scattering occurs without an energy change, Raman scattering involves a shift in energy corresponding to molecular vibrational modes. This scattering delivers important insights into the chemical composition and structural properties of the material.

As shown in Figure 5, the X-axis (Raman shift, cm^{-1}) represents the change in scattered light energy measured in reciprocal centimeters (cm^{-1}). Each vertex along this axis corresponds to a specific molecular oscillation mode in the sample.

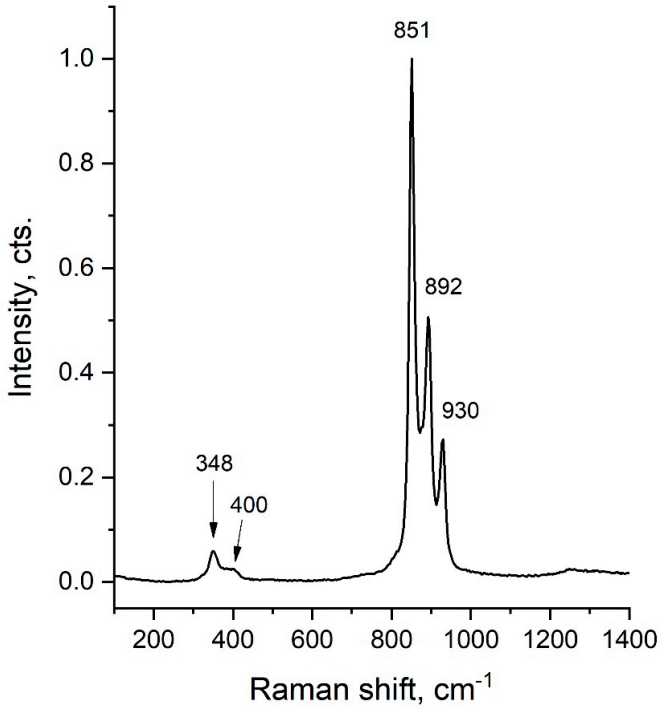


Figure 5. Spectrum of the sample ($LiCr_{3.4}Fe_{1.6}O_8$) similar to the typical spinel structure signal.

The *Y*-axis (Intensity, counts) indicates the intensity of the scattered light, which reflects the number of molecules participating in a particular vibrational mode. Higher peak intensities correspond to a larger number of molecules vibrating in that mode.

The spectrum displays several peaks with varying intensities, each representing distinct vibrational modes of the sample's molecules. For instance, the peak at 851 cm^{-1} is the most intense, signifying a dominant vibrational mode. Peaks at 892 cm^{-1} and 930 cm^{-1}, situated near the 851 cm^{-1} peak, correspond to other vibrational modes or different components within the sample. Peaks at 348 cm^{-1} and 400 cm^{-1} have lower intensities, suggesting they arise from less common vibrational modes or impurities present in the sample.

2.3. Scanning Electron Microscope

A scanning electron microscope (SEM) (APPLICATION Note Team, Bruker, Berlin, Germany) was utilized to analyze the distribution spectrum, perform both qualitative and quantitative assessments, and determine the elemental composition by percentage.

To examine the surface morphology of the newly synthesized complex mixed ferrite $LiCr_{3.4}Fe_{1.6}O_8$ samples prepared via the sol-gel method, an electron microscope capable of scanning electric diffraction images and illuminating microstructures was employed. Various parameters were calculated, all of which aligned well with the X-ray analysis results. The presence of dark regions behind the nanostructures suggests the absence of nanomaterials in those areas. Furthermore, the micrographs reveal well-formed single-phase spinel ferrites, which are ideal for applications such as microwave absorption. Electron microscopy images of the compound's surface are shown in Figure 6a–d.

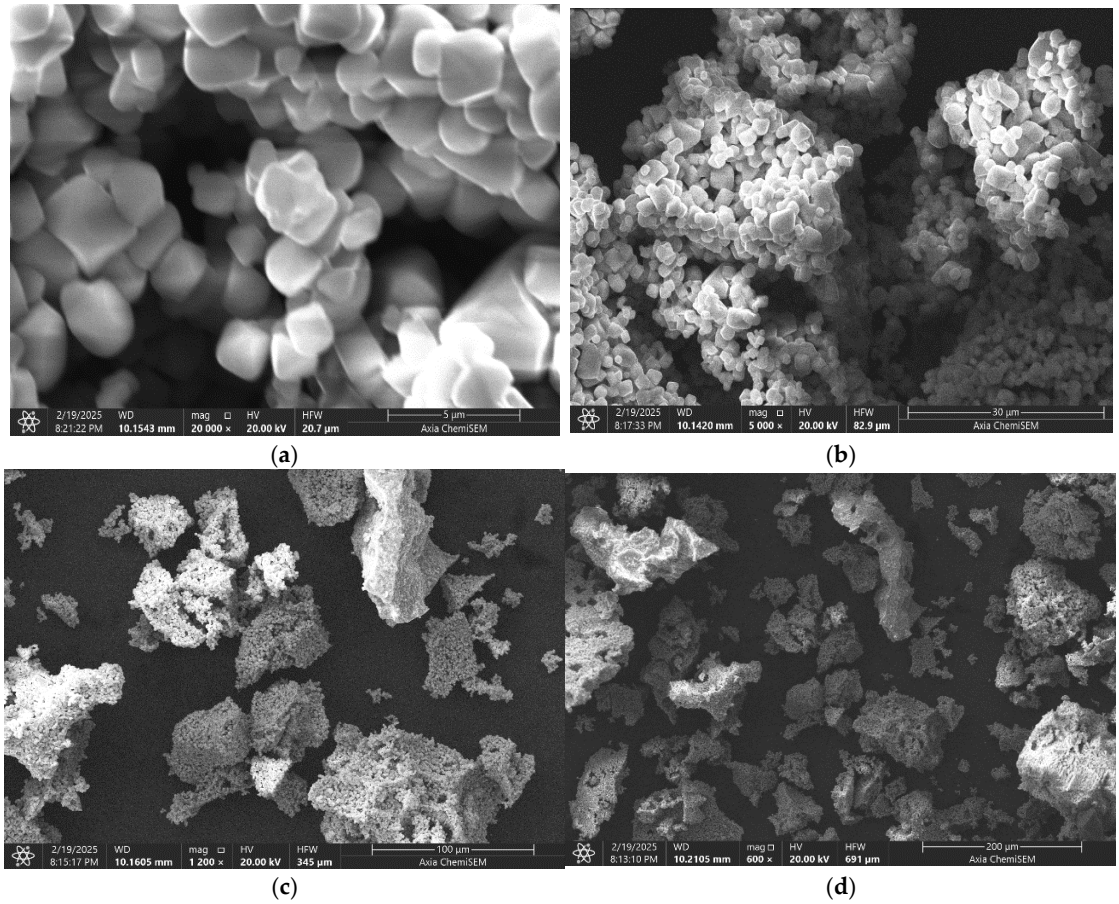


Figure 6. Micrometer-precision images of the new mixed complex ferrite $LiCr_{3.4}Fe_{1.6}O_8$ captured at four different magnification scales.

The micrographs taken at magnifications of 5, 30, 100, and 200 µm are presented above, showing the overall morphology of the surface layer of the complex ferrite. The analysis confirmed that the compound is single-phase, with its structural clarity defined by its topography and chemical composition. Figure 7 displays the spectral data and elemental analysis results for the synthesized new mixed complex ferrite $LiCr_{3.4}Fe_{1.6}O_8$.

The microstructure, chemical composition, and elemental distribution of chromium, iron, lithium, and oxygen within the sample were investigated based on the elemental mapping and crystallization characteristics. Quantitative elemental analysis reveals that iron, chromium, lithium, oxygen, and carbon atoms are distributed across regions measuring approximately 100 µm. Scanning electron microscopy also allowed observation of nanometer-sized particles within the powdered solid material.

The elemental distribution, along with quantitative and qualitative analyses, was performed using scanning electron microscopy. Figure 8 presents the spectral data of the synthesized new complex ferrite and the corresponding elemental analysis results.

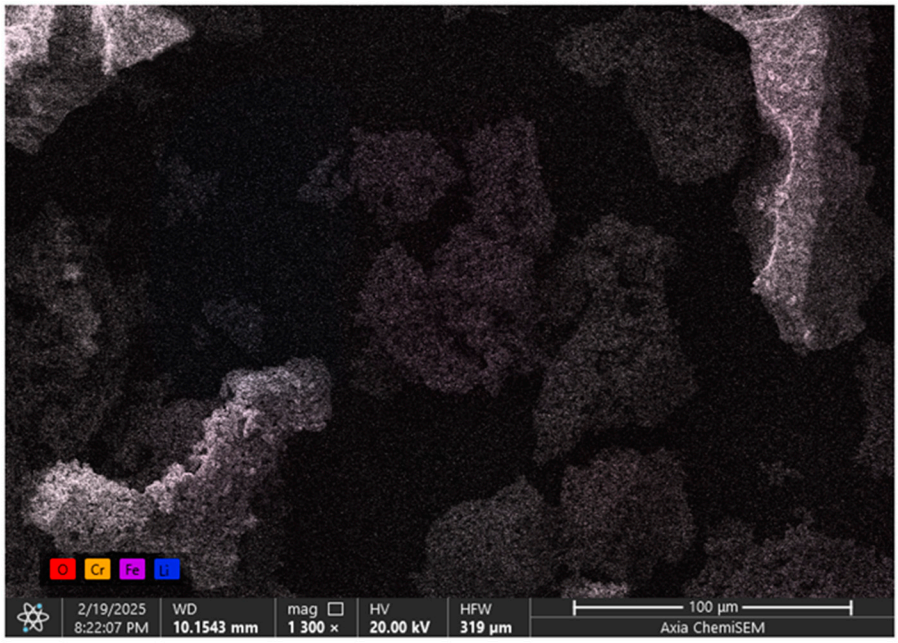
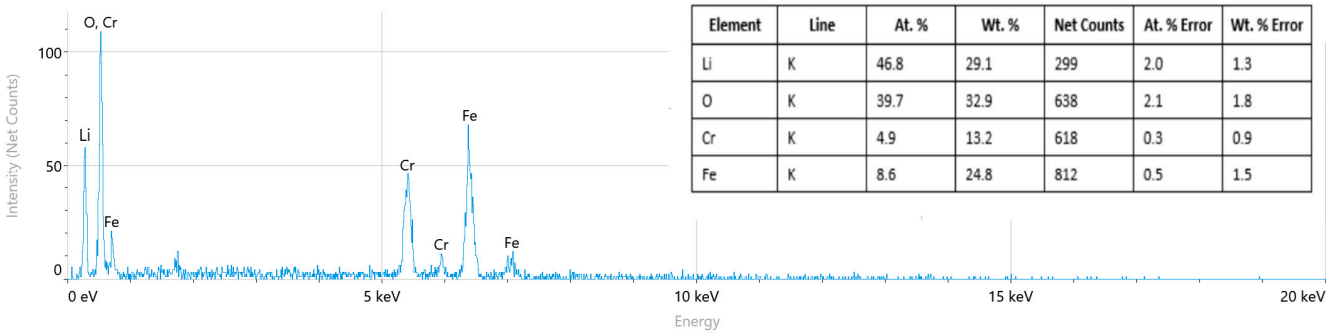


Figure 7. Distribution map of elements in the new mixed complex ferrite $LiCr_{3.4}Fe_{1.6}O_8$ (distribution order and color coding of Cr, Fe, Li, O elements in the map).



Element	Line	At. %	Wt. %	Net Counts	At. % Error	Wt. % Error
Li	K	46.8	29.1	299	2.0	1.3
O	K	39.7	32.9	638	2.1	1.8
Cr	K	4.9	13.2	618	0.3	0.9
Fe	K	8.6	24.8	812	0.5	1.5

Figure 8. Spectral samples of the $LiCr_{3.4}Fe_{1.6}O_8$ compound. Elemental analysis results are integrated.

The elemental composition and distribution of the synthesized complex ferrite $LiCr_{3.4}Fe_{1.6}O_8$ were investigated using energy-dispersive X-ray (EDX) spectroscopy. The obtained EDX spectrum confirmed the presence of the main elements—lithium (Li), chromium (Cr), iron (Fe), and oxygen (O)—consistent with the theoretical stoichiometric composition of the compound.

Quantitative analysis revealed slight deviations in the relative atomic percentages of the elements compared to the theoretical values. These differences can be attributed to the surface sensitivity of the EDX technique and the inherent difficulty in accurately detecting light elements, particularly lithium.

A comparison of theoretical and experimental data showed that the elements are uniformly distributed according to the stoichiometric ratio of the $LiCr_{3.4}Fe_{1.6}O_8$ phase, confirming the homogeneous structure of the synthesized material. In addition, the slightly higher amounts of oxygen and lithium observed in the spectrum may be associated with surface oxidation or lithium accumulation at grain boundaries.

Overall, the EDX analysis confirms that the obtained ferrite forms a single-phase spinel structure with a uniform distribution of elements.

2.4. Broad Band Spectrometer Analysis

The variation of the capacitance (Cp) of $LiCr_{3.4}Fe_{1.6}O_8$ ferrite with frequency at different temperatures is shown in Figure 9. At low frequencies, the capacitance exhibits relatively high values, while it gradually decreases as the frequency increases. This behavior can be attributed to space charge and interfacial polarization effects that dominate at low frequencies, whereas at higher frequencies, the dipoles fail to follow the alternating field, leading to a reduction in polarization. Furthermore, the increase in temperature enhances the mobility of charge carriers and the degree of polarization up to a certain limit, after which further heating results in a decrease in capacitance due to thermal vibrations and structural relaxation effects.

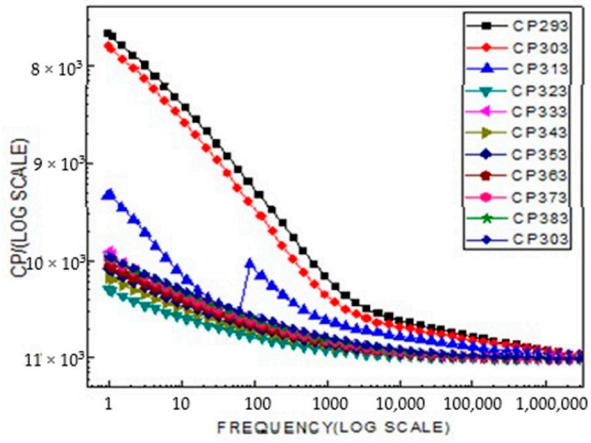


Figure 9. A part from Phil parameter, electrical conduction also increases with increase temperature.

According to the obtained results, the capacitance properties of the complex $LiCr_{3.4}Fe_{1.6}O_8$ ferrite are strongly temperature-dependent. With increasing temperature, the capacitance (Cp) of the material gradually rises and remains nearly constant up to approximately 303 °C. In this range, the increase in the thermal mobility of charge carriers and the strengthening of dipolar polarization play a key role. However, beyond 303 °C, a sharp decline in capacitance is observed. This phenomenon is associated with a reduction in defect concentration within the crystal lattice, the weakening of intergranular barrier layers, and changes in the relaxation dynamics of charge carriers under high-temperature conditions.

Overall, the obtained results indicate that the dielectric properties of $LiCr_{3.4}Fe_{1.6}O_8$ ferrite are highly sensitive to its structural stability and temperature effects. This suggests that the material holds potential for application in electronic and energy-storage devices operating in high-temperature environments.

The real part of the modulus increases similarly with frequency. The presence of two plateau regions indicates the existence of two distinct relaxation processes in the material, which are reflected by two peaks in the modulus (M) curve. The peak observed in the low-frequency region corresponds to the long-range hopping motion of charge carriers, where charges move from one ionic site to neighboring sites at the grain boundaries. In contrast, the peak appearing in the high-frequency region (observed at 313 K) is associated with short-range hopping motion, where ions are spatially confined and exhibit localized movement within the grains. As the temperature increases, the shift of this peak toward higher frequencies, as shown in Figure 10, suggests that the short-range hopping transport process becomes more dominant at elevated temperatures.

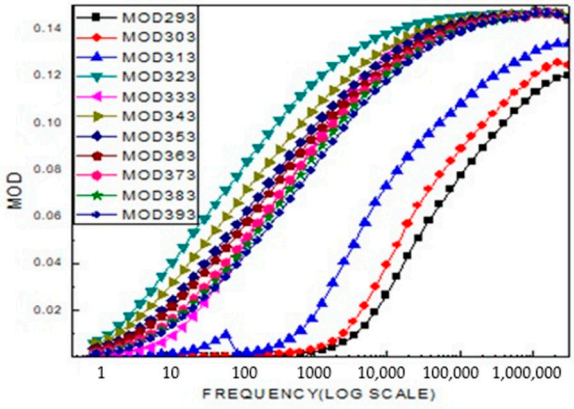


Figure 10. Shows a typical frequency dependent modulus real: M($LiCr_{3\cdot4}Fe_{1\cdot6}O_8$).

Figure 11 shows that the conductivity of the samples is nearly independent of frequency in the low-frequency region. Their high insulating nature, characterized by low conductivity values ranging from 10^2 to 10^6 S/cm, and the stability of conductivity over a wide range of low frequencies make these samples suitable materials for the fabrication of high-quality resistors.

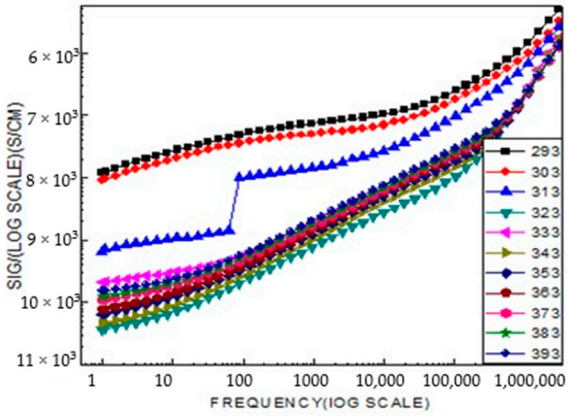


Figure 11. Shows the frequency (f) dependence of the real part σ of a.c. conductivity at selected temperatures in the range 293 K–393 K for the $LiCr_{3\cdot4}Fe_{1\cdot6}O_8$ sample.

In a wide range of ceramic materials, conduction can occur through ionic conduction, mixed ionic–electronic conduction, or purely electronic conduction, while grain boundaries act as barriers to the movement of charge carriers. This barrier effect is generally more pronounced at lower temperatures (Figure 12). In this temperature range, perovskite-type titanates such as $LiCr_{3\cdot4}Fe_{1\cdot6}O_8$ are widely used in capacitor applications as materials with high dielectric permittivity. At temperatures well above the Curie point, $LiCr_{3\cdot4}Fe_{1\cdot6}O_8$-based ceramics exhibit a pronounced effect of highly resistive grain boundaries (GB). This phenomenon is attributed to the space charge effect of a Schottky-type depletion layer. In such applications, titanates must be acceptor-doped to prevent semiconducting behavior in the ferrite materials.

Figure 13 shows the dielectric loss of the material, which is highly sensitive to both frequency and temperature. The shift of the dielectric relaxation peaks toward higher frequencies with increasing temperature clearly indicates that this process is thermally activated.

At low frequencies, the highly resistive grain boundaries exhibit reactive behavior, leading to greater absorption of electrical energy as current flows through the material. The variation in specific resistance with temperature for $LiCr_{3\cdot4}Fe_{1\cdot6}O_8$ across frequencies ranging from 1 Hz to 1 MHz is shown above. This behavior is attributed to the fact that

increasing temperature enhances the mobility of charge carriers, while the applied electric field acts as a driving force, aligning the electric dipoles in its direction. The data indicate that specific resistance decreases with increasing temperature and frequency.

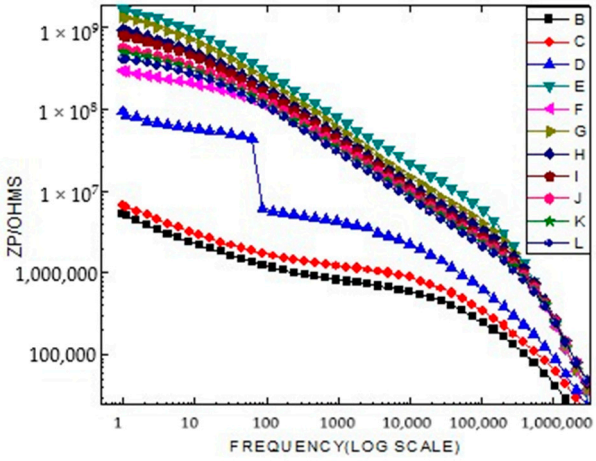


Figure 12. Grain boundaries play an important role in the electrical properties of a variety of ferrite materials and components.

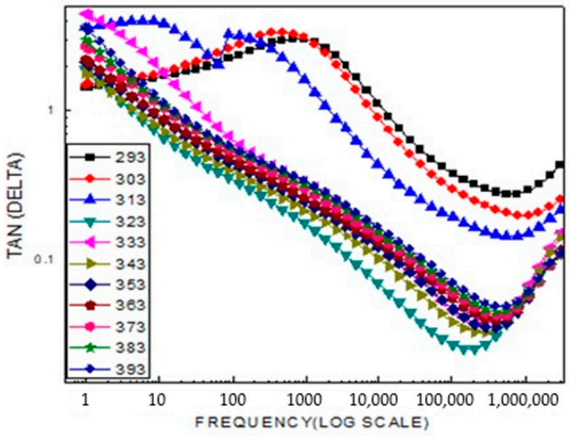


Figure 13. Dielectric loss (Tan δ) show that dielectric loss rapidly decreases with increasing frequency and fall to 1 above 100 Hz.

2.5. Electrophysical Research

The procedure followed the established methods for measuring electrophysical properties [41,42]. The dielectric constant and electrical resistance were investigated by measuring the electrical capacitance of the samples using an LCR-800 serial device (Taiwan) under thermostatic conditions at a working frequency of 1 kHz in a continuous dry air environment, with a holding time at each specified temperature.

The samples were prepared as disc-shaped pellets, parallel to the plane, with a diameter of 10 mm and a thickness ranging from 2 to 6 mm. A binder mixture (1.5%) was added prior to pressing, which was performed at a pressure of 20 kg/cm^2. The resulting discs were sintered in a SNOL laboratory furnace at 400 °C for 6 h, followed by careful surface leveling on both sides.

The dielectric constant was calculated based on the sample's capacitance, taking into account its thickness and the surface area of the electrodes. A Sawyer–Tower circuit was employed to determine the relationship between electric displacement D and electric field strength E. The hysteresis loop D was visually monitored using a C1-83 oscilloscope,

connected to a voltage divider consisting of resistances of 6 MΩ and 700 kΩ, along with a reference capacitor of 0.15 μF. The generator frequency was set to 300 Hz.

During all temperature-dependent measurements, the samples were placed inside a furnace. Temperature was monitored using a chromel–alumel (chromium–aluminum) thermocouple connected to a B2-34 voltmeter, with a measurement error of ±0.1 mV. The heating rate was maintained at 5 K/min. The dielectric constant at each temperature was calculated using the following formula:

$$\varepsilon = \frac{C}{C_0} \quad (3)$$

where C_0 is the capacitance of the capacitor without the test material (in air).

The band gap energy (ΔE) of the material under investigation was calculated using the following formula:

$$\Delta E = \frac{2kT_1T_2}{0.43(T_2 - T_1)} \log \frac{R_1}{R_2}$$

where k is the Boltzmann constant equal to 8.6173303×10^{-5} eB·K^{-1}; R_1 is the resistance at T_1; and R_2 is the resistance at T_2.

To verify the accuracy of the obtained data, the dielectric constant of a standard reference material, barium titanate ($BaTiO_3$), was measured at frequencies of 1 kHz, 5 kHz, and 10 kHz. Table 3 presents the measured electrophysical properties of $BaTiO_3$.

As shown in Table 3, the dielectric constant values of $BaTiO_3$ at 293 K for frequencies of 1 kHz and 5 kHz are in good agreement with the recommended value of 1400 ± 250. Furthermore, the observed changes in the electrical conductivity of $BaTiO_3$ at all measured frequencies (1 kHz, 5 kHz, and 10 kHz) at 383 K correspond to its phase transition from the cubic perovskite structure (space group Pm3m) to the tetragonal (polar) ferroelectric phase (space group P4mm) [43–45].

Table 3. Dependence of electrical resistance (R), electrical capacity (C), and dielectric constant (ε) on $BaTiO_3$ temperature.

T, K	C, nF	R, Ом	ε	lgε	lgR
Measurement frequency at 1 kHz					
293	0.27278	13,400	1296	3.11	4.13
303	0.27426	13,270	1303	3.11	4.12
313	0.27715	12,910	1316	3.12	4.11
323	0.28125	12,560	1336	3.13	4.10
333	0.28772	11,890	1367	3.14	4.08
343	0.29313	11,210	1392	3.14	4.05
353	0.29916	10,290	1421	3.15	4.01
363	0.30751	9383	1461	3.16	3.97
373	0.31202	8831	1482	3.17	3.95
383	0.31702	9061	1506	3.18	3.96
393	0.32255	8814	1532	3.19	3.95
403	0.32967	7881	1566	3.19	3.90
413	0.3423	7098	1626	3.21	3.85
423	0.35119	6902	1668	3.22	3.84
433	0.36668	6153	1742	3.24	3.79
443	0.38018	6317	1806	3.26	3.80
453	0.39802	6010	1891	3.28	3.78
463	0.4169	5584	1980	3.30	3.75
473	0.43147	5149	2050	3.31	3.71
483	0.45456	4656	2159	3.33	3.67

Table 3. *Cont.*

T, K	C, nF	R, Ом	ε	lgε	lgR
Measurement frequency at 5 kHz					
293	0.25678	29,630	1220	3.09	4.47
303	0.2683	21,650	1274	3.11	4.34
313	0.2775	13,080	1318	3.12	4.12
323	0.28638	5236	1360	3.13	3.72
333	0.29667	4301	1389	3.14	3.63
343	0.30226	4733	1409	3.15	3.68
353	0.30787	3296	1436	3.16	3.52
363	0.31283	2966	1462	3.17	3.47
373	0.31843	2805	1486	3.17	3.45
383	0.32148	2529	1513	3.18	3.40
393	0.32578	2669	1527	3.18	3.43
403	0.32976	3172	1547	3.19	3.50
413	0.33303	4434	1566	3.19	3.65
423	0.33948	6377	1582	3.20	3.80
433	0.35613	9644	1613	3.21	3.98
443	0.3713	11,520	1692	3.23	4.06
453	0.3925	10,430	1764	3.25	4.02
463	0.41682	8021	1864	3.27	3.90
473	0.44245	5978	1980	3.30	3.78
483		3799	2102	3.32	3.58
Measurement frequency at 10 kHz					
293	0.11814	152,300	561	2.75	5.18
303	0.18494	70,790	878	2.94	4.85
313	0.22927	32,200	1089	3.04	4.51
323	0.25954	11,870	1233	3.09	4.07
333	0.27501	4842	1306	3.12	3.69
343	0.28531	3312	1355	3.13	3.52
353	0.29302	2689	1392	3.14	3.43
363	0.29988	2257	1424	3.15	3.35
373	0.30652	1946	1456	3.16	3.29
383	0.31215	1689	1483	3.17	3.23
393	0.31667	1737	1504	3.18	3.24
403	0.32294	3130	1534	3.19	3.50
413	0.32779	5945	1557	3.19	3.77
423	0.33406	8231	1587	3.20	3.92
433	0.34256	8805	1627	3.21	3.94
443	0.35658	8052	1694	3.23	3.91
453	0.378	5967	1796	3.25	3.78
463	0.39475	4604	1875	3.27	3.66
473	0.41687	3343	1980	3.30	3.52
483	0.44203	2353	2100	3.32	3.37

It is worth noting that although a decrease in the dielectric constant of $BaTiO_3$ was recorded at 10 kHz and temperatures of 293 K, 303 K, and 313 K, the dielectric constant (ε) values across the full temperature range of 313–483 K remain as high as approximately 2150 at all three frequencies (1 kHz, 5 kHz, and 10 kHz). This indicates that frequency variation within this range has little impact on the temperature dependence of the dielectric constant for $BaTiO_3$.

Electrophysical measurements for $LiCr_{3\cdot4}Fe_{1\cdot6}O_8$ were performed using the LCR setup over the temperature range of 293–483 K at frequencies of 1, 5, and 10 kHz (see Table 4 and Figure 14).

The data presented in Tables 4 and 5 and Figure 14 indicate that the dielectric permittivity (ε) of material 1 at 293 K is relatively high, measured at 2.69 × 10^5, and it reaches a peak value of 2.47 × 10^6 at 373 K. As the temperature further increases to the range of 423–483 K, the ε values decrease significantly, dropping to 122 at 483 K. Additionally, increasing the frequency to 10 kHz causes a reduction in ε throughout the entire temperature range (293–483 K).

Table 4. Dependence of electrical capacity (C), electrical resistance (R), and dielectric constant (ε) of $LiCr_{3.4}Fe_{1.6}O_8$ on temperature and frequency.

T, K	C, nF	R, Ом	ε	Lgε	lgR
Measurement frequency at 1 kHz					
293	7.7977	165,700	22,448	4.35	5.22
303	10.302	135,800	29,658	4.47	5.13
313	15.68	101,700	45,140	4.65	5.01
323	12.489	131,900	35,954	4.56	5.12
333	8.1684	203,600	23,515	4.37	5.31
343	14.516	121,200	41,789	4.62	5.08
353	86.933	32,510	250,266	5.40	4.51
363	176.65	19,300	508,547	5.71	4.29
373	265.14	14,110	763,295	5.88	4.15
383	378.56	10,520	1,089,813	6.04	4.02
393	495.27	8184	1,425,802	6.15	3.91
403	312.87	10,720	900,702	5.95	4.03
413	11.039	85,500	31,779	4.50	4.93
423	1.8105	379,400	5212	3.72	5.58
433	0.95809	649,900	2758	3.44	5.81
443	0.68585	843,600	1974	3.30	5.93
453	0.70009	874,900	2015	3.30	5.94
463	0.89737	796,100	2583	3.41	5.90
473	1.3483	666,100	3882	3.59	5.82
483	2.1329	511,600	6140	3.79	5.71
Measurement frequency at 5 kHz					
293	1.3926	140,100	4009	3.60	5.15
303	1.8886	115,400	5437	3.74	5.06
313	2.728	89,690	7853	3.90	4.95
323	1.517	128,100	4367	3.64	5.11
333	0.9064	184,900	2609	3.42	5.27
343	2.5719	93,070	7404	3.87	4.97
353	15.47	29,090	44,536	4.65	4.46
363	31.031	17,900	89,333	4.95	4.25
373	45.909	13,060	132,165	5.12	4.12
383	64.608	9799	185,996	5.27	3.99
393	82.944	7702	238,782	5.38	3.89
403	40.501	11,420	116,596	5.07	4.06
413	1.7403	79,660	5010	3.70	4.90
423	0.28075	293,500	808	2.91	5.47
433	0.13233	455,500	381	2.58	5.66
443	0.09429	533,500	271	2.43	5.73
453	0.09084	555,900	262	2.42	5.74
463	0.10483	536,400	302	2.48	5.73
473	0.13985	477,500	403	2.60	5.68
483	0.19866	401,900	572	2.76	5.60

Table 4. *Cont.*

T, K	C, nF	R, Ом	ε	Lgε	lgR
Measurement frequency at 10 kHz					
293	0.62512	126,300	1800	3.26	5.10
303	0.85581	103,700	2464	3.39	5.02
313	1.188	83,510	3420	3.53	4.92
323	0.50394	127,500	1451	3.16	5.11
333	0.3238	169,200	932	2.97	5.23
343	1.2082	76,460	3478	3.54	4.88
353	7.2162	26,640	20,774	4.32	4.43
363	14.584	16,680	41,985	4.62	4.22
373	21.676	12,440	62,402	4.80	4.09
383	30.192	9304	86,918	4.94	3.97
393	39.355	7426	113,297	5.05	3.87
403	14.483	12,940	41,694	4.62	4.11
413	0.64942	83,960	1870	3.27	4.92
423	0.12128	243,700	349	2.54	5.39
433	0.06145	329,700	177	2.25	5.52
443	0.04865	351,900	140	2.15	5.55
453	0.04694	362,500	135	2.13	5.56
463	0.05137	360,400	148	2.17	5.56
473	0.06369	339,200	183	2.26	5.53
483	0.08415	306,100	242	2.38	5.49

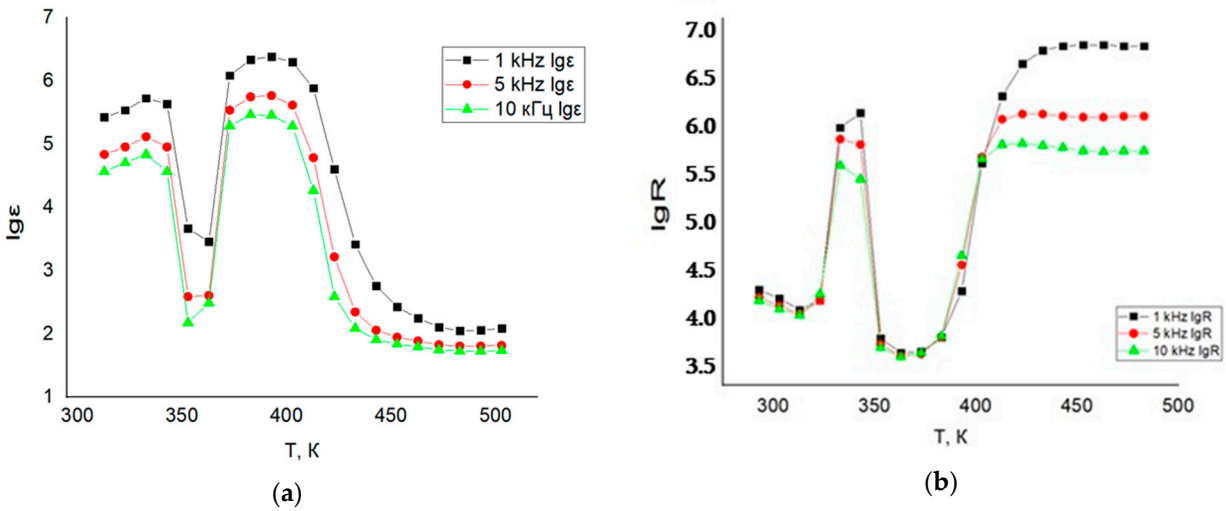


Figure 14. Temperature and frequency (1 kHz, 5 kHz, and 10 kHz) dependence of the dielectric permittivity (**a**) and electrical resistance (**b**) of $LiCr_{3.4}Fe_{1.6}O_8$.

Table 5. (**a**). Calculation of the band gap width (ΔE) in the range of 293–313 K. (**b**). Calculation of the band gap width (ΔE) in the range of 343–363 K.

(a)	
T, K	**lg R**
293	4.41
313	4.22
(b)	
T, K	**lg R**
343	6.10
363	3.81

The temperature dependence of electrical resistance reveals complex conductivity behavior: from 293 K to 313 K, the material behaves like a semiconductor; between 313 K and 343 K, it exhibits metallic conduction; from 343 K to 363 K, it returns to semiconductor-like behavior; and from 363 K to 483 K, it again shows metallic conductivity.

$$\Delta E = \frac{2 \times 0.00086173 \times 293 \times 313}{0.43(313 - 293)} log \frac{4.41}{4.22} = 1.92\ B$$

$$\Delta E = \frac{2 \times 0.000086173 \times 343 \times 363}{0.43(363 - 343)} log \frac{6.10}{3.81} = 4.0\ B$$

3. Discussion

A comprehensive investigation of the structural and physical properties of the $LiCr_{3\cdot4}Fe_{1\cdot6}O_8$ sample confirmed the formation of a well-defined cubic spinel structure. The average crystallite size was determined to be 5.2 nm using the Scherrer equation and 9.12 nm from the Williamson–Hall analysis, while the calculated microstrain ($\varepsilon = 1.71 \times 10^{-3}$) indicated lattice distortion associated with the incorporation of Cr^{3+} ions. Raman spectra exhibited characteristic vibrational modes: Li^+, Cr^{3+}, and Fe^{3+} ions near 200 cm^{-1}, Fe–O stretching vibrations within 500–600 cm^{-1}, and Cr–O vibrations in the 600–700 cm^{-1} range. A sharp band at approximately 720 cm^{-1} further confirmed the high degree of structural ordering in the ferrite phase. SEM micrographs revealed uniformly distributed nanostructured grains, while elemental mapping (Cr, Fe, Li, O) demonstrated a homogeneous distribution of the constituent elements, confirming the effectiveness of the synthesis process. Dielectric measurements showed that the dielectric constant (ε') increased with rising temperature, reaching a maximum value of ~2.5×10^6 in the range of 353–373 K. Conversely, ε' decreased with increasing frequency, which can be attributed to Maxwell–Wagner interfacial polarization and hopping conduction of charge carriers. Furthermore, the dielectric loss (tan δ) exhibited a decreasing trend with frequency, indicating that the material displays stable and typical dielectric behavior.

4. Materials and Methods

The sol–gel method was utilized as an efficient technique for synthesizing a novel complex mixed ferrite with a heterogeneous composition. To identify the composition of the synthesized ferrite, X-ray (Osaka, Japan) phase analysis was performed. Scanning electron microscopy (SEM) (Waltham, MA, USA) was used for both qualitative and quantitative characterization of the material. In addition, the electrophysical properties, such as dielectric conductivity and electrical resistivity, were thoroughly investigated.

The crystal structure of lithium chromium ferrite powder samples was examined using X-ray diffraction (XRD) analysis. Phase identification was carried out with a Rigaku Miniflex/600 (Tokyo, Japan) diffractometer, operating with CuKα radiation (U = 30 kV, I = 10 mA), a scanning speed of 1000 pulses per second, and a time constant of 5 s. Data were collected over a 2θ range of 5° to 90° and analyzed using the PDF-5+ database.

The synthesis process began with high-purity reagent-grade chromium (III) oxide, iron (III) oxide, and lithium carbonate as the primary raw materials, along with distilled water. Glycerol (a trihydric alcohol) and citric acid served as the gel-forming agents. The stoichiometric amounts of the raw materials were precisely weighed to an accuracy of 0.0001 g using an analytical balance, followed by mixing and grinding in an agate mortar. The prepared mixture was then transferred to an alumina crucible and dried at 100 °C in an electric furnace to promote gel formation.

After drying, the gel was subjected to calcination at 600 °C in a muffle furnace for 6 h, resulting in the formation of a fine black powder. This powder was then sintered in air,

with the temperature gradually increased from 700 °C to 1000 °C over a total duration of 30 h, using 6-h increments at each temperature step [46].

The pycnometric density of the ferrite samples was determined using the liquid displacement method [47], employing toluene and deionized water as inert displacement fluids. Each sample's density was measured five times, and the average values were calculated to ensure accuracy.

5. Conclusions

In conclusion, the novel mixed complex ferrite with the composition $LiCr_{3.4}Fe_{1.6}O_8$ was successfully synthesized for the first time using the sol-gel method. To characterize the new complex ferrite, X-ray phase analysis, scanning electron microscopy (for both qualitative and quantitative elemental analysis), and electrophysical property measurements (including dielectric constant and electrical resistance) were performed.

For the first time, X-ray phase analysis was used to determine the symmetry types and unit cell parameters of the synthesized complex ferrite. The compound $LiCr_{3.4}Fe_{1.6}O_8$ was identified as cubic (a = b = c = 8.3001 Å, Z = 2) with calculated and pycnometric densities of 4.745 g/cm^3 and 4.748 g/cm^3, respectively. The X-ray results confirmed that the synthesized material is polycrystalline, and the crystallographic data accuracy is supported by the close agreement between X-ray and pycnometric densities.

Raman spectroscopy was employed to study the vibrational modes of the molecules. The presence of characteristic Fe–O and Cr–O vibrational peaks confirmed that the $LiCr_{3.4}Fe_{1.6}O_8$ sample possesses a spinel-type structure. Variations in intensity and peak positions among the spectra suggest sample heterogeneity or differing crystal orientations in various regions. The Raman spectrum indicated a complex phase composition, including spinel structures and ferrite groups.

Scanning electron microscopy allowed the collection of micro-samples from different regions of the $LiCr_{3.4}Fe_{1.6}O_8$ crystals for elemental composition analysis. The overall morphology of the complex ferrite's surface was observed, confirming that the compound is single-phase. The structure was further elucidated by the topography and chemical composition analysis. The elemental analysis results, presented in tabular form, confirmed the formula $LiCr_{3.4}Fe_{1.6}O_8$. The particle sizes ranged from 5 μm to 200 μm.

Electrophysical studies showed that the $LiCr_{3.4}Fe_{1.6}O_8$ ferrite's capacitance and conductivity increase with temperature. The material exhibits two distinct relaxation mechanisms depending on frequency: long-range hopping at low frequencies and short-range hopping at high frequencies. At low frequencies, the material exhibits low conductivity, making it suitable for resistor applications. Grain boundaries contribute high resistance at elevated temperatures, while dielectric losses decrease with increasing frequency. The real part of the resistance decreases with both temperature and frequency, indicating the material's potential use in electronic devices.

Electrophysical measurements of $LiCr_{3.4}Fe_{1.6}O_8$ were conducted over the temperature range of 293–483 K at frequencies of 1, 5, and 10 kHz. At 293 K and 1 kHz, the dielectric constant (ε) was 2.69×10^5, reaching a maximum of 2.47×10^6 at 373 K. Increasing the frequency to 10 kHz resulted in a decrease in ε across the entire temperature range studied.

The temperature dependence of electrical resistance revealed complex conductivity behavior: semiconductor-like conductivity from 293 to 313 K, metallic behavior between 313 and 343 K, semiconductor-like again from 343 to 363 K, and metallic conduction from 363 to 483 K. The band gap was measured to be 1.92 eV within the 293–313 K range, typical of narrow-gap semiconductors, while at 343–363 K, it increased to 4.0 eV, characteristic of wide-gap semiconductors.

Overall, the obtained results suggest that $LiCr_{3.4}Fe_{1.6}O_8$ ferrite is a promising material for potential applications in electronics and energy storage devices.

Author Contributions: Conceptualization, M.M., A.M., and K.R.; methodology, M.A., B.K. and K.S.; software, Z.T.; validation, A.M., M.A., and Z.T.; formal analysis, M.N.; investigation, A.M.; resources, M.M. and M.A.; data curation, M.M.; writing—original draft preparation, A.M. and M.A.; writing—review and editing, M.M.; visualization, A.K.; and Z.T.; supervision, M.M. and M.A.; project administration, A.M. and M.N. All authors have read and agreed to the published version of the manuscript.

Funding: This study was funded by the research project AP26198947 "Synthesis and study of the properties of multicomponent perovskites for the development of magnetically sensitive media with controlled physico-chemical characteristics".

Institutional Review Board Statement: Not applicable.

Informed Consent Statement: Not applicable.

Data Availability Statement: The original contributions presented in the study are included in the article; further inquiries can be directed to the corresponding author.

Conflicts of Interest: The authors declare no conflicts of interest. The funders had no role in the design of the study; in the collection, analyses, or interpretation of data; in the writing of the manuscript, or in the decision to publish the results.

References

1. Mataev, M.M.; Madiyarova, A.M.; Patrin, G.S.; Abdraimova, M.R.; Nurbekova, M.A.; Tursunova, Z.I. Synthesis and physico–chemical characteristics of complex ferrite $CrNaFe_2O_5$. *Chem. J. Kaz.* **2024**, *1*, 109–118. [CrossRef]
2. Mataev, M.M.; Madiyarova, A.M.; Patrin, G.S.; Abdraimova, M.R.; Nurbekova, M.A.; Durmenbayeva, Z.D. Synthesis of New Complex Ferrite $Li_{0.5}MnFe_{1.5}O_4$: Chemical–Physical and Electrophysical Research. *Materials* **2024**, *17*, 3754. [CrossRef]
3. Saad, A.A.; Khan, W.; Dhiman, P.; Naqvi, A.H.; Singh, M. Structural, optical and magnetic properties of perovskite $(La_{1-x}\ Sr_{\ x})(Fe_{1-x}\ Ni_x)O_3$, (x = 0.0, 0.1 & 0.2) nanoparticles. *Electron. Mater. Lett.* **2013**, *9*, 77–81.
4. Benali, A.; Azizi, S.; Bejar, M.; Dhahri, E.; Graça, M.F.P. Structural, electrical and ethanol sensing properties of double-doping $LaFeO_3$ perovskite oxides. *Ceram. Int.* **2014**, *40*, 14367–14373. [CrossRef]
5. Ming, Q.; Nersesyan, M.D.; Wagner, A.; Ritchie, J.; Richardson, J.T.; Luss, D.; Jacobson, A.J.; Yang, Y.L. Combustion synthesis and characterization of Sr and Ga doped $LaFeO_3$. *Solid State Ion.* **1999**, *122*, 113–121. [CrossRef]
6. Zhaisanbaeva, M.E.; Patrin, G.S.; Seitbekova, K.S.; Nurbekova, M.A.; Mataev, M.M. Synthesis and Structural Studies of Perovskite-Ytterbium Manganate and Spinel-Cobalt Chromite Nanomaterials. *Eng. Sci.* **2025**, *34*, 1469. [CrossRef]
7. Khetre, S.M.; Jadhav, H.V.; Jagadale, P.N.; Kulalb, S.R.; Bamane, S.R. Studies on electrical and dielectric properties of $LaFeO_3$. *Adv. Appl. Sci. Res.* **2011**, *2*, 503–511.
8. Sora, I.N.; Fontana, F.; Passalacqua, R.; Ampelli, C.; Perathoner, S.; Centi, G.; Parrino, F.; Palmisano, L. Photoelectrochemical properties of doped lanthanum orthoferrites. *Electrochim. Acta* **2013**, *109*, 710–715. [CrossRef]
9. Varandili, S.B.; Babaei, A.; Ataie, A.; Khodadadi, A.A.; Kazerooni, H. Nano-structured Pd doped $LaFe(Co)O_3$ perovskite; synthesis, characterization and catalytic behavior. *Mater. Chem. Phys.* **2018**, *205*, 228–239. [CrossRef]
10. Mataev, M.M.; Abdraimova, M.R.; Tursinova, Z.I.; Kezdikbaeva, A.T. Thermodynamic Properties of Complex, Ferrite $BiCa_3Fe_5O_{12}$. *Orient. J. Chem.* **2017**, *33*, 3200–3203. [CrossRef]
11. Fujii, T.; Matsusue, I.; Takada, J. Superparamagnetic Behaviour and Induced Ferrimagnetism of $LaFeO_3$ Nanoparticles. *Adv. Asp. Spectrosc.* **2012**, 373–390. [CrossRef]
12. Haye, E.; Capon, F.; Barrat, S.; Boulet, P.; Andre, E.; Carteret, C.; Bruyere, S. Properties of rare-earth orthoferrites perovskite driven by steric hindrance. *J. Alloys Compd.* **2016**, *657*, 631–638. [CrossRef]
13. Deraz, N.M.; Shaban, S. Optimization of catalytic, surface and magnetic properties of nanocrystalline manganese ferrite. *J. Anal. Appl. Pyrolysis.* **2009**, *86*, 173–179. [CrossRef]
14. Deraz, N.M.; El-Aiash, M.K.; Ali, S.A. Novel preparation and physicochemical characterization of a nanocrystalline cobalt ferrite system. *Adsorpt. Sci. Technol.* **2009**, *27*, 797–810. [CrossRef]
15. Deraz, N.M.; Alarifi, A.; Shaban, S.A. Removal of sulfur from commercial kerosene using nanocrystalline $NiFe_2O_4$ based sorbents. *J. Saudi Chem. Soc.* **2010**, *14*, 357–362. [CrossRef]

16. Köseoğlu, Y.; Baykal, A.; Gözüak, F.; Kavas, H. Structural and magnetic properties of $Co_xZn_{1-x}Fe_2O_4$ nanocrystals synthesized by microwave method. *Polyhedron* **2009**, *28*, 2887–2892. [CrossRef]
17. Mataev, M.M.; Myrzakhmetova, N.O.; Kuanysheva, Z.K.; Saparbekova, I.S.; Bazilbayev, S.M.; Doszhanova, G.A.; Medeuova, G. Calorimetric and Thermodynamic Studies of Complex Ferrites in the Temperature Range of 298, 15-673 K. *Orient. J. Chem.* **2015**, *31*, 441–445. [CrossRef]
18. Cao, S.-W.; Zhu, Y.-J.; Cheng, G.-F.; Huang, Y.-H. $ZnFe_2O_4$ nanoparticles: Microwave-hydrothermal ionic liquid synthesis and photocatalytic property over phenol. *J. Hazard. Mater.* **2009**, *171*, 431–435. [CrossRef]
19. Zhou, Z.H.; Xue, J.M.; Wang, J.; Chan, H.S.O.; Yu, T.; Shen, Z.X. $NiFe_2O_4$ nanoparticles formed in situ in silica matrix by mechanical activation. *J. Appl. Phys.* **2002**, *91*, 6015. [CrossRef]
20. Köseoğlu, Y.; Yıldız, F.; Slazar-Alvarez, G.; Toprak, M.; Muhammed, M.; Aktaş, B. Synthesis, characterization and ESR measurements of CoNiO nanoparticles. *Phys. Status Solidi* **2005**, *42*, 1712–1718. [CrossRef]
21. Zhang, L.; Wang, Y.; Liu, B.; Wang, J.; Han, G.; Zhang, Y. Characterization and property of magnetic ferrite ceramics with interesting multilayer structure prepared by solid-state reaction. *Ceram. Int.* **2021**, *47*, 10927–10939. [CrossRef]
22. Jabbarzare, S.; Abdellahi, M.; Ghayour, H.; Arpanahi, A.; Khandan, A. A study on the synthesis and magnetic properties of the cerium ferrite ceramic. *J. Alloys Compd.* **2017**, *694*, 800–807. [CrossRef]
23. Samir Ullah, M.; Firoz Uddin, M.; Momin, A.A.; Hakim, M.A. Effect of V_2O_5 addition on the structural and magnetic properties of Ni–Co–Zn ferrites. *Mater. Res. Express.* **2021**, *8*, 016102. [CrossRef]
24. Tatarchuk, T.; Myslin, M.; Mironyuk, I.; Bououdina, M.; Pędziwiatr, A.T.; Gargula, R.; Bogacz, B.F.; Kurzydło, P. Synthesis, morphology, crystallite size and adsorption properties of nanostructured Mg–Zn ferrites with enhanced porous structure. *J. Alloys Compd.* **2020**, *819*, 152945. [CrossRef]
25. Ghodake, U.R.; Kambale, R.C.; Suryavanshi, S.S. Effect of Mn^{2+} substitution on structural, electrical transport and dielectric properties of Mg–Zn ferrites. *Ceram. Int.* **2017**, *43*, 1129–1134. [CrossRef]
26. Farid, H.M.T.; Ahmad, I.; Ali, I.; Ramay, S.M.; Mahmood, A.; Murtaza, G. Dielectric and impedance study of praseodymium substituted Mg-based spinel ferrite. *J. Magn. Magn. Mater.* **2017**, *434*, 143–150. [CrossRef]
27. Rathod, V.; Anupama, A.V.; Jali, V.M.; Hiremath, V.A.; Sahoo, B. Combustion synthesis, structure and magnetic properties of Li–Zn ferrite ceramic powders. *Ceram. Int.* **2017**, *43*, 14431–14440. [CrossRef]
28. Phanidhar Varma, P.V.S.K.; Suryanarayana, B.; Raghavendra, V.; Parajuli, D.; Murali, N. Effect of cr substitution on magnetic properties of cocu nano ferrites. *Solid State Technol.* **2022**, *63*, 8820–8827.
29. Kharabe, R.G.; Devan, R.S.; Kanamadi, C.M.; Chougule, B.K. Dielectric properties of mixed Li–Ni–Cd ferrites. *Smart Mater. Struct.* **2006**, *15*, N36. [CrossRef]
30. Sánchez, R.D.; Rivas, J.; Vaqueiro, P.; López-Quintela, M.A.; Caeiro, D. Particle size effects on magnetic properties of yttrium iron garnets prepared by a sol–gel method. *J. Magn. Magn. Mater.* **2002**, *247*, 92–98. [CrossRef]
31. Mataev, M.M.; Abdraimova, M.R.; Saxsena, S.S.; Kezdikbaeva, A.T. Synthesis and X-ray analysis of complex ferrites $BiMe_3^{II}Fe_5O_{12}$ (MII = Mg, Ca, Ba). *Key Eng. Mater.* **2017**, *744*, 393–398. [CrossRef]
32. Parajuli, D.; Murali, N.; Samatha, K.; Veeraiah, V. Thermal, structural, morphological, functional group and first cycle charge/discharge study of co substituted $LiNi_{1X-0.02}Mg_{0.02}Co_XO_2$ (x = 0.00, 0.02, 0.04,0.06, and 0.08) cathode material for libs. *AIP Adv.* **2022**, *12*, 085010. [CrossRef]
33. Parajuli, D.; Taddesse, P.; Murali, N.; Veeraiah, V.; Samatha, K. Effect of Zn^{2+} doping on thermal, structural, morphological, functional group, and electrochemical properties of layered $LiNi_{0.8}Co_{0.1}Mn_{0.1}O_2$ cathode material. *AIP Adv.* **2022**, *12*, 125012. [CrossRef]
34. Parajuli, D.; Samatha, K. Structural and cation distribution analysis of Nickel-Copper/Nickel-Magnesium substituted Lithium Ferrites. *Bibechana* **2024**, *21*, 74–82. [CrossRef]
35. Mataev, M.M.; Patrin, G.S.; Abdraymova, M.R.; Tursinova, Z.I.; Yurkin, G.Y. Synthesis and magnetic properties of crystals $Bi_2BaFe_4O_{10}$. *J. Sib. Fed. Univ.—Math. Phys.* **2018**, *11*, 411–415. [CrossRef]
36. Nath, D.; Singh, F.; Das, R. X-ray diffraction analysis by Williamson-Hall, Halder-Wagner and size-strain plot methods of CdSe nanoparticles- a comparative study. *Mater. Chem. Phys.* **2020**, *239*, 122021. [CrossRef]
37. Manh, D.H.; Ngoc Nha, T.T.; Hong Phong, L.T.; Nam, P.H.; Thanh, T.D.; Phong, P.T. Determination of the crystalline size of hexagonal $La_{1-x}Sr_xMnO_3$ (x = 0.3) nanoparticles from X-ray diffraction—A comparative study. *RSC Adv.* **2023**, *13*, 25007–25017. [CrossRef] [PubMed]
38. Mustapha, S.; Ndamitso, M.M.; Abdulkareem, A.S.; Tijani, J.O.; Shuaib, D.T.; Mohammed, A.K.; Sumaila, A. Comparative study of crystallite size using Williamson-Hall and Debye-Scherrer plots for ZnO nanoparticles. *Adv. Nat. Sci. Nanosci. Nanotechnol.* **2019**, *10*, 045013. [CrossRef]
39. Paswan, S.K.; Kumari, S.; Kar, M.; Singh, A.; Pathak, H.; Borah, J.P.; Kumar, L. Optimization of structure-property relationships in nickel ferrite nanoparticles annealed at different temperature. *J. Phys. Chem. Solids* **2021**, *151*, 109928. [CrossRef]
40. Narang, S.B.; Pubby, K. Nickel spinel ferrites: A review. *J. Magn. Magn. Mater.* **2021**, *519*, 167163. [CrossRef]

41. Okazaki, K. *Technology of Ceramic Dielectrics*; Energiya: Moscow, Russia, 1976; 256p.
42. Kasenov, B.K.; Kasenova, S.B.; Sagintaeva, Z.I.; Baisanov, S.; Lu, N.Y.; Nukhuly, A.; Kuanyshbekov, E.E. Heat Capacity and Thermodynamic Functions of Titanium-Manganites of Lanthanum, Lithium and Sodium of $LaLi_2TiMnO_6$ and $LaNa_2TiMnO_6$. *Molecules* **2023**, *28*, 5194. [CrossRef] [PubMed]
43. Fesenko, E.G. *The Perovskite Family and Ferroelectricity*; Atomizdat: Moscow, Russia, 1972.
44. Venevtsev, Y.N.; Politova, E.D.; Ivanov, S.A. *Ferroelectric and Antisegnetoelectrics of the Barium Titanate Family*; Chemistry: Moscow, Russia, 1985.
45. Lines, M.; Glass, A. *Ferroelectrics and Related Materials*; Mir: Moscow, Russia, 1981.
46. Mataev, M.M.; Abdraimova, M.R.; Nuketaeva, D.Z.; Kezdikbaeva, A.T. $YbBiNaFeO_5$ Compound-Ferrite Extraction Method. Patent of the Republic of Kazakhstan No. 104109, 28 April 2018.
47. Mataev, M.; Sarsenbaeva, Z.; Keskin, B.; Nurbekova, M.; Meldeshov, A.; Tursyn, Z.; Seitbekova, K. Synthesis, Structure, and Electrophysical and Electrochemical Properties of Novel Composite $La_{0.9}MnO_3$-$LaFeO_3$. *Molecules* **2025**, *30*, 132. [CrossRef] [PubMed]

Disclaimer/Publisher's Note: The statements, opinions and data contained in all publications are solely those of the individual author(s) and contributor(s) and not of MDPI and/or the editor(s). MDPI and/or the editor(s) disclaim responsibility for any injury to people or property resulting from any ideas, methods, instructions or products referred to in the content.